ACS OMEGA

http://pubs.acs.org/journal/acsodf

Article

Enhanced H_2S Gas-Sensing Performance of Ni-Doped ZnO Nanowire Arrays

Shaoyu Liu, Weiye Yang, Lei Liu, Huohuo Chen, and Yingkai Liu*

Cite This: *ACS Omega* 2023, 8, 7595−7601

Read Online

ACCESS | Metrics & More | Article Recommendations | Supporting Information

ABSTRACT: Ni-doped ZnO nanowire arrays (Ni−ZnO NRs) with different Ni concentrations are grown on etched fluorine-doped tin oxide electrodes by the hydrothermal method. The Ni−ZnO NRs with a nickel precursor concentration of 0−12 at. % are adjusted to improve the selectivity and response of the devices. The NRs' morphology and microstructure are investigated by scanning electron microscopy and high-resolution transmission electron microscopy. The sensitive property of the Ni−ZnO NRs is measured. It is found that the Ni−ZnO NRs with an 8 at. % Ni precursor concentration have high selectivity for H_2S and a large response of 68.9 at 250 °C compared to other gases including ethanol, acetone, toluene, and nitrogen dioxide. Their response/recovery time is 75/54 s. The sensing mechanism is discussed in terms of doping concentration, optimum operating temperature, gas type, and gas concentration. The enhanced performance is related to the regularity degree of the array and the doped Ni^{3+} and Ni^{2+} ions, which increases the active sites for oxygen and target gas adsorption on the surface.

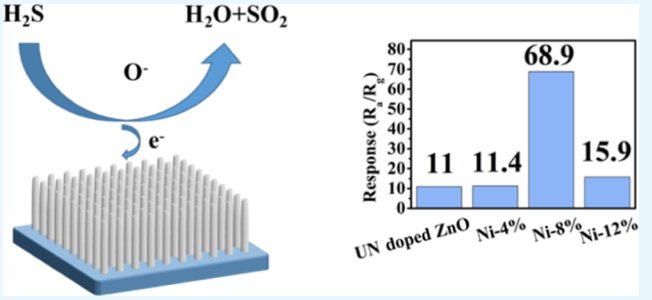

1. INTRODUCTION

Due to the rapid development of industrialization and urbanization, toxic and hazardous gases have posed a great threat to the ecosystem. Among them, the detection and continuous monitoring of volatile organic compounds (VOCs) and toxic gases has become a top priority in society's efforts to provide a safe and healthy environment.[1−3] H_2S is a highly toxic gas, and even small amounts inhaled will cause death in a short time.[4−6] Even low concentrations of inhalation will have some effect on the eyes, respiratory system, and central nervous system.[7−9] However, VOCs are widely presented in the decomposition of organic compounds, the placement of sewage, and the biogas produced by landfill sites.[10,11] It is crucial to monitor them in daily life. Among the existing gas sensors, metal oxides are widely used because of their high sensitivity, low cost, flexible production methods, and compatibility with electronic devices.[12,13] ZnO, as a typical n-type semiconductor, has received much attention because it owns high electron mobility and photoelectric response, chemical stability, and thermal stability.[14] ZnO is employed in various scenarios including solar cells,[15] photocatalysis,[16] optoelectronic devices, and gas sensors.[17−20] More and more researchers have devoted themselves to the research and development of metal oxide sensors since Katoch et al. developed a simple ZnO gas sensor in 1971. M. R. Modaberi prepared a Ni-doped ZnO nanorod as a H_2S sensor with a response of 45.3 to 100 ppm H_2S at 200 °C.[21] Bhati et al. synthesized reduced graphene oxide (rGO) nanosheets (0, 0.04, 0.11, 0.17, and 1.04 wt % rGO-ZnO) to nanofibers to detect NO_2 by electrostatic spinning and found that 0.04 wt % rGO-ZnO exhibited the highest performance at 400 °C to 5 ppm NO_2.[22] The above-mentioned work revealed that doping played an effect on the performance of ZnO gas sensors.[23−28] In this work, ZnO NRs are fabricated on etched FTO electrodes by a hydrothermal method and the composition of Ni (0−12 at. %) in ZnO NRs is controlled by means of a bimetallic-organic precursor in a single hybridization. Multitudinous characterization approaches are employed to explore the morphology, microstructure, elemental composition, and valence state of the samples. A series of the Ni-doped ZnO nanowire array (Ni−ZnO NR) sensors are developed to monitor H_2S. Compared to the pure counterpart, it revealed that the obtained Ni−ZnO NRs with an 8 at. % nickel precursor concentration (hereafter denoted as the 8 at. % Ni−ZnO NRs) have the strongest responsivity.

2. EXPERIMENTAL DETAILS

2.1. Synthesis of ZnO NP Gas Sensors. The growth mode is as follows.[29] The etched FTO electrodes were used as the gas-sensitive electrodes. The etched channel was 1 mm in

Received: November 3, 2022
Accepted: January 20, 2023
Published: February 20, 2023

https://doi.org/10.1021/acsomega.2c07092
ACS Omega 2023, 8, 7595−7601

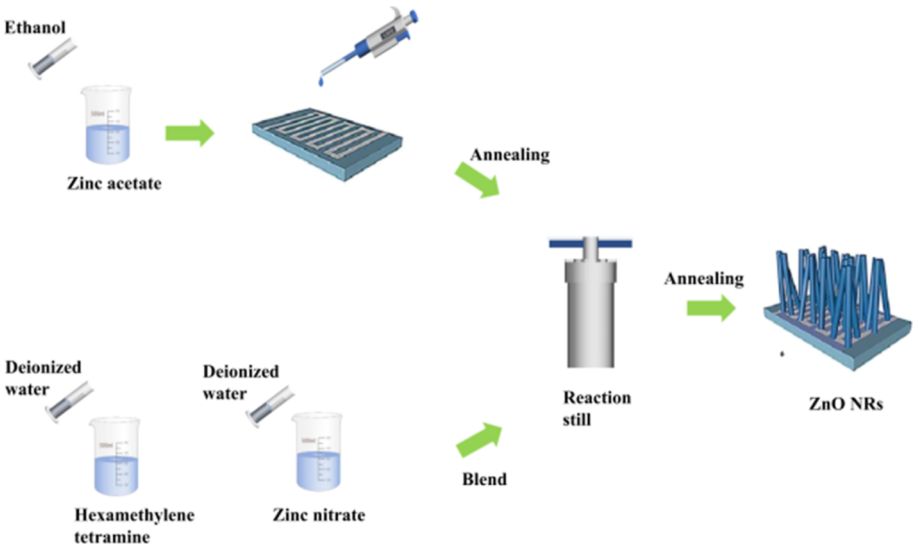

Figure 1. Preparation of the ZnO NR sensor.

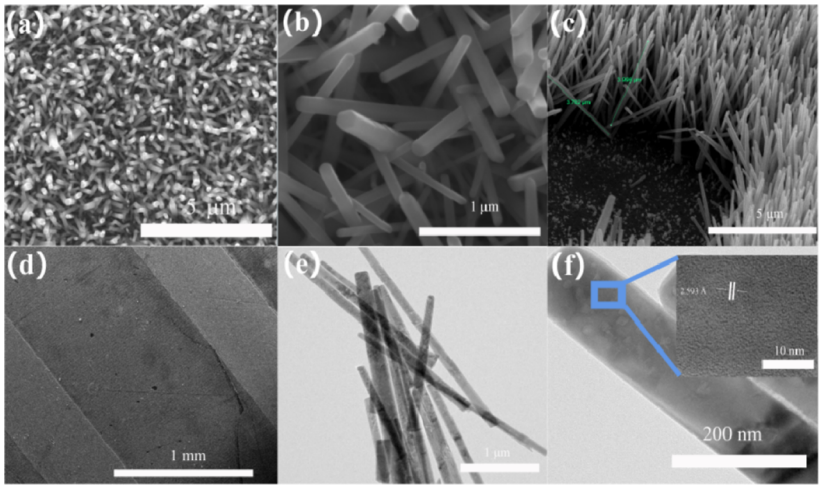

Figure 2. SEM, TEM, and HRTEM images of 8 at. % Ni−ZnO NRs. (a,b) Top view SEM images at low and high magnifications. (c) Side view of the SEM images. (d) SEM image of the etched FTO electrodes. (e) TEM image. (f) HRTEM image.

length with a width of 0.5 mm. Before preparing the ZnO sensors, the etched FTO electrodes were washed with acetone, ethanol, as well as deionized water for 10 min by ultrasonication and then blown dry by a nitrogen gun and placed in a blast drying oven for 20 min. After that, the electrode was put into the plasma cleaning instrument for 10 min.

The sensors of ZnO NRs were prepared in situ on electrodes using a simple drop coating technique and the hydrothermal method. The gas-sensitive electrode was placed on a horizontal surface. Then, 0.02 g of a seed solution was placed on the center of the electrode using a capillary tube with approximately 1 mm diameter. The electrodes were put into a blast dryer for 20 min and then annealed in a tube furnace at 350 °C for 20 min. In this way, we obtained a uniform seed layer growing on the surface of the etched FTO electrodes. The treated electrodes were then placed into the reactor. Second, a 0.25 M aqueous solution of hexamethylenetetramine and a 0.25 M aqueous solution of $Zn(NO_3)_2{\cdot}6H_2O$ (99.0%) were put into the inner liner of Teflon in the ratio of 1:1. The reactions were carried out in an autoclave at 95 °C for 3 h. We removed the sample and cleaned it with deionized water after the reactor had naturally cooled to room temperature. After that, the cleaned electrodes were placed in a tube furnace and annealed at 400 °C for 60 min. We repeated this proceed three times in order to obtain longer and more homogeneous nanowire arrays. Consequently, the ZnO NRs on the etched FTO electrodes were fabricated and annealed at 650 °C for 1 h to obtain the device.

In addition, we further fabricated Ni−ZnO NRs with different concentrations via a single hybridized bimetallic-organic precursor approach. Different concentrations of $Zn(NO_3)_2{\cdot}6H_2O$ (99.0%) to $Ni(NO_3)_2{\cdot}6H_2O$ (99.0%) to replace a 0.25 M aqueous solution of $Zn(NO_3)_2{\cdot}6H_2O$ (99.0%) were used. The precursor solution produced in the above step was used as the starting precursor to prepare Ni-doped ZnO NRs with different concentrations in the above-mentioned manner.

The production flow chart of Ni-doped ZnO NRs is shown in Figure 1.

2.2. Material Characterization. X-ray photoelectron spectroscopy (XPS, Kα, America) was conducted in an ion-pumped chamber. The morphologies of the samples were

https://doi.org/10.1021/acsomega.2c07092
ACS Omega 2023, 8, 7595−7601

characterized by field-emission scanning electron microscopy (Quanta FEG 250, America) and transmission electron microscopy (TEM, Tecnai G2 F20 S-TWIN instrument with a field emission gun at 20 kV).

2.3. Measurement of the Gas Sensors. The sensing property of the device was measured using an intelligent gas-sensitive analysis system (CGS-1TP). The process was as follows: first, the sensor was put on a hot table at 250 °C for 48 h. Then, the sensor was connected to the platform electrodes to form a closed loop. The steps for gas response measurements were as follows: (1) the prepared device was placed on a test bench; (2) after tying the probe to the etched FTO electrode to form a loop, the cap was closed to form a closed system, and the R_g value was recorded; (3) a certain amount of the gas was injected into the evaporation tray to fill the entire cavity. The resistance of the sensor changed. Finally, the cavity cover was removed for desorption.[30] All measurements were performed in a well-ventilated laboratory. The dehumidifier retained the relative humidity at 45%. The sensor's response is defined as the ratio of exposure resistance of the ZnO NP sensor in air (R_a) to the resistance of the target gas in the atmosphere (R_g) and can be expressed as

$$S = \frac{R_a}{R_g} \quad (1)$$

3. RESULTS AND DISCUSSION

3.1. Structure and Morphology. The morphology and microstructure of the 8 at. % Ni−ZnO NRs are investigated by SEM and TEM. Figure 2a,b shows the top view SEM images of the 8 at. % Ni−ZnO NRs at low and high magnifications. It revealed that the large area and homogeneous structures of NRs were successfully synthesized. Figure 2c shows the side view by SEM of the sample. It can be noted that the nanowires have a good array structure with a length of 3−4 μm. Figure 2d shows the SEM image of the Ni−ZnO NRs on the etched FTO electrodes. It is observed that our Ni−ZnO NRs evenly grow on an intercalated electrode, in which the etched channel is 1 mm in length with an electrode width of 0.5 mm. We can further observe that the NRs were distributed sparsely on the channel. Figure 2e shows the TEM image of the NRs, indicating that every NR has a smooth surface with a uniform diameter. Figure 2f shows the high-resolution TEM (HRTEM) image of a single Ni−ZnO NR at the cylindrical rod junction. The NR consists of small and uniform arrangements of a uniform rod-like structure, and the array structure is more conducive to efficient electron transfer. Figure 2f shows a clear lattice stripe with a 0.2593 nm spacing distance, corresponding to the (002) plane of ZnO. The small and sparse structure of ZnO NRs is more conducive to their making full contact with the gas and improving its sensitivity.

The chemical states of the atoms in the samples are determined by XPS. Figure 3a shows the survey scan XPS spectra of the Ni−ZnO NRs and the undoped counterpart. The constituent elements of the Zn 2p, Ni 2p, and O 1s peaks are detected. The binding energies obtained in the XPS data are standardized for specimen charging using C 1s as the reference at 284.8 eV. Figure 3b shows the Zn 2p peaks for all samples. Compared to the undoped counterpart, the Zn $2p_{3/2}$ and Zn $2p_{1/2}$ nuclear energy levels are centered around 1021.28 and 1043.68 eV, respectively. However, the Ni-doped ZnO nuclear energy levels undergo a shift of 0−0.7 eV toward

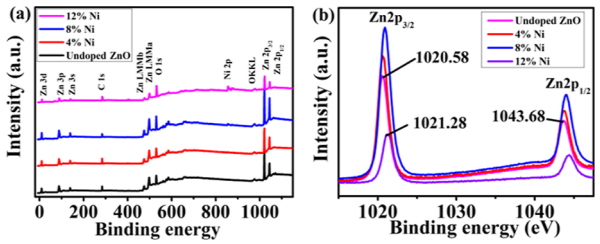

Figure 3. XPS spectra of ZnO and Ni−ZnO NRs with Ni precursor concentrations of 4, 8, and 12 at. %. Full spectra of (a) undoped and Ni-doped ZnO NRs and (b) Zn $2p_{3/2}$ and Zn $2p_{1/2}$.

a high energy. The peak difference (23.1 eV) in the spin orbit splitting energy between the two nuclear energy levels remains unchanged.

The binding energy spectra of O 1s for the different samples are shown in Figure 5a−d, in which the O 1s peak was

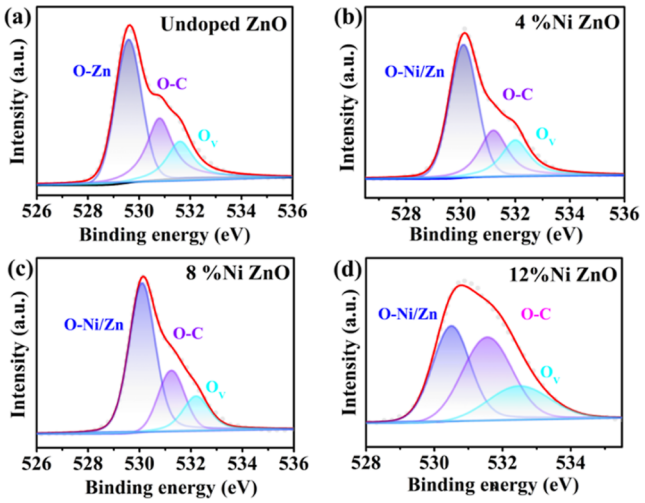

Figure 4. (a−d) O states of undoped and Ni−doped ZnO NRs.

deconvoluted into three sub-peaks. Figure 5a−d shows that these three peaks can be divided into two types: the regular lattice sites[31] and hypoxic sites (O_V).[32] The O_L is divided into two types, O−Zn/Ni and O−C. The O_V intensity ratio increases with the increase of doping concentration. It is also found that with an increase of doping concentration, the peak area O_V to O 1s ratios of the Ni−ZnO NRs to that of the pure counterpart are 5.7, 5.2, 6.8, and 5.0, respectively, revealing that doping effectively increases the amount of anoxia to (O_V). Therefore, from the analysis of O 1s, the 8 at. % Ni−ZnO NRs having more abundant O_V should have better performance, which is consistent with our test results.

Figure 6a−c shows that the Ni concentrations in the precursor solution are 4, 8, and 12 at. % in ZnO NRs. Figure 6a−c shows the curves with Ni $2p_{3/2}$, Ni $2p_{1/2}$, and shakeup satellite peaks. The Ni $2p_{3/2}$ peak at 855.28 eV in Figure 6b can be divided into two sub-peaks, corresponding to Ni^{2+} and Ni^{3+} valence states, respectively. The nickel ions are mainly present in the divalent state in ZnO NRs at lower nickel concentrations. However, the proportion of the trivalent state increases with increasing nickel content. The spin−orbit splitting energy is 17.36 eV, being different from 17.8 eV of metallic Ni, certifying that the nickel has successfully taken the place of zinc, and the reason for this phenomenon is the

https://doi.org/10.1021/acsomega.2c07092
ACS Omega 2023, 8, 7595−7601

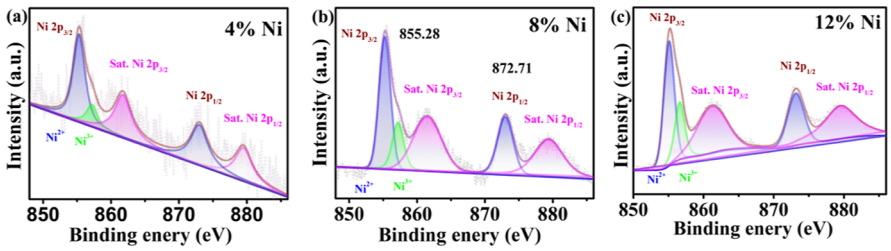

Figure 5. (a–c) XPS spectra of ZnO and Ni–ZnO NRs with Ni precursor concentrations of 4, 8, and 12 at. %.

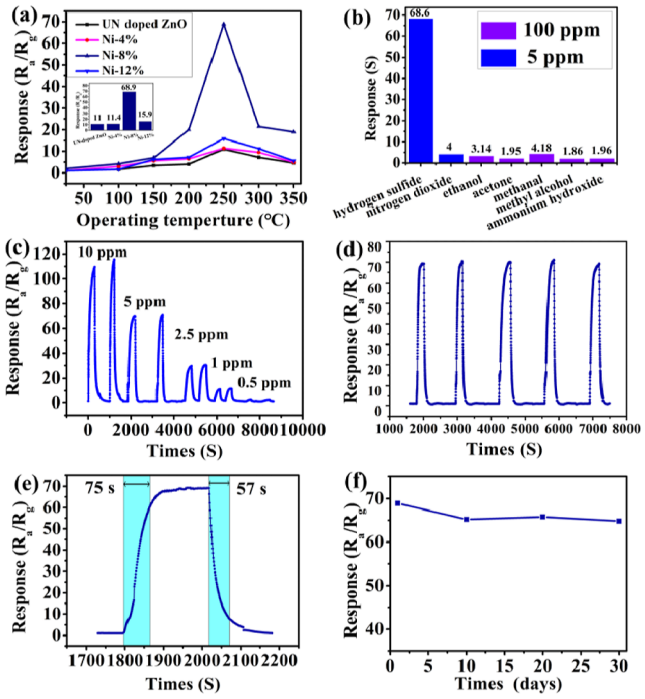

Figure 6. Sensitive properties of the Ni–ZnO NRs and undoped counterpart. (a) Response versus temperature (T) to 5 ppm H_2S; inset: response comparison of four samples at 250 °C. (b) Selectivity of 8 at. % Ni–ZnO NRs to different gases. (c) Dynamic response of 8 at. % Ni–ZnO NRs. (d,e) Cyclic stability of 8 at. % Ni–ZnO NRs and the single-set desorption curve at 250 °C. (f) Long-term stability of 8 at. % Ni–ZnO NRs for 30 days.

charge-transfer leap of the O 2p and Ni 3d hybridization in the final state.

According to the references, it can be concluded theoretically that the presence of an appropriate content of Ni^{2+} in ZnO will reduce the activation energy of H_2S gas adsorption, which is also the reason why doping can improve the performance. The formation of a small amount of Ni^{3+} is caused by the defect of hydrothermal growth. Moreover, the content of Ni^{3+} is less than that of Ni^{2+}, so it does not play a major role in this process.

We also performed an EDX analysis of the material as shown in the Supporting Information Figure S1. As shown in Figure S1, we can see that Ni element is successfully doped into the ZnO material. It can be further demonstrated that the materials prepared in this paper have a uniform distribution of Zn, Ni, and O elements.

As shown in the Supporting Information Figure S2, we have performed X-ray diffraction spectra of four materials with different Ni doping concentrations in the range of 30–70°. The detection results demonstrate the ZnO (JCPDS card no. 36-1451) (100), (002), (101), (102), (110), and (103) facets corresponding to the hexagonal fibrillated zincite structure. The reason for this phenomenon is that the small amount of Ni element does not constitute the cluster structure of NiO but replaces the lattice position of Zn and does not change the crystal structure of the material. This phenomenon also indicates that the single-source metal precursor-induced growth method used in this paper can effectively dope Ni into ZnO NRs.

3.2. Gas-Sensitive Performance Analysis. Figure 4a shows the sensitive performance of the Ni–ZnO NRs with (0 to 12%) Ni precursor concentration to 5 ppm H_2S at 90–350 °C. The response increases with increasing temperature up to 250 °C, which is the optimum work temperature, indicating that the fastest surface chemistry has good carrier mobility. At above 250 °C, oxygen desorption may be faster than oxygen adsorption and thus less adsorbed oxygen molecules are available to react with the target gas, resulting in a decrement in response at higher temperatures.[33,34] The increasing temperature accelerates the electron leap between the conductor band and the surface Fermi energy level, which facilitates the desorption reaction.[35]

The responses for undoped and Ni–ZnO NRs at 250 °C for 5 ppm H_2S gas are presented in the inset of Figure 6a. This shows that the response is the highest for ZnO NRs grown in a precursor solution with a Ni concentration of 8 at. % Ni–ZnO NRs, and the response to H_2S is improved by a factor of 6.24 compared to that of the pure ZnO NRs. It is worthy of attention that the response of the 8 at. % Ni–ZnO NRs is enhanced in a non-linear manner. Moreover, the performance of the gas-sensitive material decreases when the doping concentration continues to increase. As the Ni concentration increases the proportion of Ni^{3+} ions increases supersaturation can form a stable structure with more oxygen. Therefore, when the Ni concentration is greater than 8%, O_V decreases instead. The reason is that the change in O_V concentration is caused by Ni doping. The XPS results show a decrease in the O_V concentration of the material at a concentration of 12%.

The following tests are conducted at 250 °C. Figure 6b shows the responses of the 8 at. % Ni–ZnO NRs to 5 ppm H_2S as well as NO_2 and 100 ppm VOCs. It is seen that the device has a good selectivity for H_2S, resulting in better adaptability in practical applications.

Figure 6b shows the response of the 8 at. % Ni–ZnO NRs to different VOCs and toxic gases. They exhibit excellent selectivity to H_2S. To evaluate their performance with respect to H_2S, Figure 6c shows their response in the range of 0.5–10 ppm. Two cycles of testing are carried out for different concentrations of the gas, and we can see a good positive correlation between the response and the gas concentration as the H_2S concentration increases from 0.5 to 10 ppm. We also

https://doi.org/10.1021/acsomega.2c07092
ACS Omega 2023, 8, 7595–7601

Table 1. Comparison of the Reported H_2S Sensing Performances Based on Different Nanostructures and This Work

sensing materials	operating temperature (°C)	concentration (ppm)	response	LOD (ppm)	references
Ni doping-ZnO nanorods	200	100	45.6		38
ZnO-rGO	RT	20	14.9	8	39
ZnO/CuO hollow	170	50	66.6	0.05	40
α Fe_2O_3 nanoparticles	300	10	5.3	0.05	41
ZnO nanorod-bundle	350	50	3		37
CuO NP decorated porous ZnO NRs	100	200	4.69		42
CdS/CdO	400	5	73.5	0.01	43
CuO	150	10	76.5		44
ZnO−$ZnFe_2O_4$	250	10	84.5		45
Cr_2O_3	170	100	42.81		46
Ni-doped ZnO NRs	250	5	68.9	0.003	this study

calculated the theoretical limits of H_2S using the signal-to-noise ratio, which are expressed as follows

$$V_{\chi^2} = \sum (y_i - y)^2 \quad (2)$$

$$\mathrm{rms}_{\mathrm{noise}} = \sqrt{\frac{V_{\chi^2}}{N}} \quad (3)$$

$$\mathrm{LOD\ (ppm)} = 3\frac{\mathrm{rms}}{\mathrm{slope}} \quad (4)$$

The calculation yields a detection limit of 3.41 ppb for the 8 at. % Ni−ZnO NRs.

Figure 6d shows a five-cycle test of the gas-sensitive performance of the device at 5 ppm. It is found that the device has good cycling stability. Figure 4e shows the response/recovery time to 5 ppm H_2S at 250 °C. The response/recovery time is 75/57 s. The response time on attachment and the recovery time on desorption are dependent on the gas concentration, type, working temperature, and doping concentration. The results for all H_2S concentrations show that higher temperatures lead to a faster response and recovery time, thus reducing the response time. The rapid response/recovery course at higher temperatures can be attributed to faster surface chemistry, enhanced gas phase diffusion, and higher charge carrier mobility. The long-term stability of the sensor is evaluated over a period of 40 days, and the results are shown in Figure 6f. Its response fluctuated between 62 and 68.9 to 15 ppm H_2S over a long period. It is also found that the test environment also had an effect on the performance of the device. The sensor is stored at atmosphere conditions for the duration of the test and is not treated in a special way, suggesting that the device has good stability.

The operating temperature is an important parameter for gas sensors. Different temperatures have significant effects on the surface state of the material. At lower temperatures, the molecules do not have sufficient active energy to adsorb onto the sensing channels of the material, resulting in a lower response.[36] As the operating temperature increases, adsorption gradually changes from physical to chemisorption, providing higher energy levels accompanied with a different charge transfer. Chemisorption at relatively high temperatures has two kinds of mechanisms for two gases that work together in this process, one is an oxidizing gas O_2 and the other is a reducing gas, such as H_2S, which can occur on the surface as follows

$$O_2(g) + 2e^- \leftrightarrow O^-(\mathrm{ads}) \quad (5)$$

$$H_2S(g) + 3O^-(\mathrm{ads}) \rightarrow H_2O(g) + SO_2(g) + 3e^- \quad (6)$$

The property of sensitivity to most metal oxide semiconductors is related to the oxygen ions adsorbed on the surface of the sensor.[37] Oxygen molecules are absorbed on the surface, and electrons in the conduction band of the metal oxide are trapped by the absorbed oxygen molecules, forming negatively charged chemisorbed oxygen ions as they are exposed to air. Depending on the operating temperature, oxygen ions may take different forms. It takes less time to reach thermal equilibrium because H_2S possesses a lower adsorption energy, but the true reaction rate depends on the concentration of H_2S in the gas and the effective surface location where it can be captured. The reaction involved in the adsorption of H_2S gas is chemisorption. Its activation energy can be determined from the Arrhenius equation: $R = R_0 \exp(-E/kT)$. Based on Modaberi's work,[38] it is known that Ni doping can effectively reduce the activation energy of H_2S adsorption at all temperatures. The activation energy of adsorption increases with the increase of Ni content when the content of Ni is greater than 8%, which is consistent with our performance test results.

As shown in Table 1, we have analyzed the performance of similar oxide semiconductor substrate H_2S detectors. After comparison, it is found that compared with other sensors of the same type, it has a higher response value and a lower detection limit at the best operating temperature. It provides a better choice for H_2S gas detection.

4. CONCLUSIONS

In this paper, we successfully synthesized Ni-doped ZnO NRs with different concentrations using a precursor solution with bimetallic hexamethyl-hypotetra as a single source. The method can selectively control the atomic ratio of Ni to Zn in double-click metal but also has the advantages of low cost, high yield, short reaction time, and chemical safety. The XPS results indicate that the nickel element effectively replaces the zinc lattice in the material. A series of characterization examinations revealed that the 8 at. % Ni−ZnO NRs had abundant oxygen vacancies, excellent thermal stability, and a large specific surface area. Gas sensitivity indicated that the sensor had a response (68.9) and faster response/recovery (79/54 s) to 5 ppm H_2S, whose response is 6.26 times as large as that of the pure sample. In addition, the detection limit of our device is 3.41 ppb, ensuring long-term detection of H_2S and ppb-level detection in practical applications. Therefore, the concept of increasing the oxygen vacancies in the material by adding a moderate amount of doping to improve the gas-sensitive properties can be extended to other gas-sensitive

https://doi.org/10.1021/acsomega.2c07092
ACS Omega 2023, 8, 7595−7601

materials. This also provides a new option for H_2S gas detection.

■ ASSOCIATED CONTENT

Supporting Information

The Supporting Information is available free of charge at https://pubs.acs.org/doi/10.1021/acsomega.2c07092.

Details of materials required for additional experiments; EDX point scan of 8 at. % Ni−ZnO NRs; and XRD patterns of the as-grown un-doped and Ni-doped ZnO NRs (PDF)

■ AUTHOR INFORMATION

Corresponding Author

Yingkai Liu − *Yunnan Key Laboratory of Opto-electronic Information Technology, Yunnan Normal University, Kunming 650500, China; Institute of Physics and Electronic Information and Key Laboratory of Advanced Technique & Preparation for Renewable Energy Materials, Ministry of Education, Yunnan Normal University, Kunming 650500, China;* orcid.org/0000-0001-6691-8605; Phone: +86-871-6594-1166; Email: ykliu@ynnu.edu.cn

Authors

Shaoyu Liu − *Yunnan Key Laboratory of Opto-electronic Information Technology, Yunnan Normal University, Kunming 650500, China; Institute of Physics and Electronic Information, Yunnan Normal University, Kunming 650500, China;* orcid.org/0000-0003-1257-4514

Weiye Yang − *Yunnan Key Laboratory of Opto-electronic Information Technology, Yunnan Normal University, Kunming 650500, China; Institute of Physics and Electronic Information, Yunnan Normal University, Kunming 650500, China;* orcid.org/0000-0001-5685-5727

Lei Liu − *Yunnan Key Laboratory of Opto-electronic Information Technology, Yunnan Normal University, Kunming 650500, China; Institute of Physics and Electronic Information, Yunnan Normal University, Kunming 650500, China*

Huohuo Chen − *Yunnan Key Laboratory of Opto-electronic Information Technology, Yunnan Normal University, Kunming 650500, China; Institute of Physics and Electronic Information, Yunnan Normal University, Kunming 650500, China;* orcid.org/0000-0003-1625-5959

Complete contact information is available at: https://pubs.acs.org/10.1021/acsomega.2c07092

Author Contributions

S.Y.L. and Y.K.L. performed the experimental design and analysis and wrote the manuscript, W.Y.Y. contributed to the preparation of the devices and obtaining SEM measurements, and H.Z. and H.H.C. contributed to analyzing data and sensing measurements. All authors have read and approved the final manuscript.

Funding

This work is funded by the National Natural Science Foundation of China (grant nos. 11764046, 12264056, and 62164013) and Yunnan Expert Workstation Project (202205AF150008).

Notes

The authors declare no competing financial interest.

Availability of data and materials; all data are fully available without restriction from the corresponding author on reasonable request.

■ ABBREVIATIONS

VOCs, volatile organic compounds; XPS, X-ray photoelectron spectroscopy; FESEM, field-emission scanning electron microscopy; TEM, transmission electron microscopy; NRs, nanowire arrays; LODs, limits of detection

■ REFERENCES

(1) Fine, G. F.; Cavanagh, L. M.; Afonja, A.; Binions, R. Metal oxide semi-conductor gas sensors in environmental monitoring. *Sensors* **2010**, *10*, 5469−5502.

(2) Wetchakun, K.; Samerjai, T.; Tamaekong, N.; Liewhiran, C.; Siriwong, C.; Kruefu, V.; Wisitsoraat, A.; Tuantranont, A.; Phanichphant, S. Semiconducting metal oxides as sensors for environmentally hazardous gases. *Sens. Actuators, B* **2011**, *160*, 580−591.

(3) Choi, J. K.; Hwang, I. S.; Kim, S. J.; Park, J. S.; Park, S. S.; Jeong, U.; Kang, Y. C.; Lee, J. H. Design of selective gas sensors using electrospun Pd-doped SnO2 hollow nanofibers. *Sens. Actuators, B* **2010**, *150*, 191−199.

(4) Guo, Z.; Chen, G.; Zeng, G.; Liu, L.; Zhang, C. Metal oxides and metal salt nanostructures for hydrogen sulfide sensing: mechanism and sensing performance. *RSC Adv.* **2015**, *5*, 54793−54805.

(5) Hosseini, Z.; zad, A.; Mortezaali, A. Room temperature H2S gas sensor based on rather aligned ZnO nanorods with flower-like structures. *Sens. Actuators, B* **2015**, *207*, 865−871.

(6) Zhang, X.; Tang, Y. Y.; Qu, S. Q.; Da, J. W.; Hao, Z. P. H2S-Selective Catalytic Oxidation: Catalysts and Processes. *ACS Catal.* **2015**, *5*, 1053−1067.

(7) Guo, K.; Wen, J.; Zhao, Y.; Wang, Y.; Zhang, Z.; Li, Z.; Qian, Z. Optimal Packing of a Rotating Packed Bed for H2S Removal. *Environ. Sci. Technol.* **2014**, *48*, 6844−6849.

(8) Ling, A. L.; Robertson, C. E.; Harris, J. K.; Frank, D. N.; Kotter, C. V.; Stevens, M. J.; Pace, N. R.; Hernandez, M. T. Carbon dioxide and hydrogen sulfide associations with regional bacterial diversity patterns in microbially induced concrete corrosion. *Environ. Sci. Technol.* **2014**, *48*, 7357−7364.

(9) Nielsen, A. H.; Vollertsen, J.; Jensen, H. S.; Madsen, H. I.; Hvitved-Jacobsen, T. Aerobic and Anaerobic Transformations of Sulfide in a Sewer System-Field Study and Model Simulations. *Water Environ. Res.* **2008**, *80*, 16−25.

(10) Li, Z. J.; Xiao, Y. L.; Xue, W. J.; Yang, Q. Y.; Zhong, C. L. Ionic Liquid/Metal-Organic Framework Composites for H2S Removal from Natural Gas: A Computational Exploration. *J. Phys. Chem. C* **2015**, *119*, 3674−3683.

(11) Zhang, J.; Dubey, B.; Townsend, T. Effect of Moisture Control and Air Venting on H2S Production and Leachate Quality in Mature C&D Debris Landfills. *Environ. Sci. Technol.* **2014**, *48*, 11777−11786.

(12) Shin, J.; Choi, S. J.; Lee, I.; Youn, D. Y.; Park, C. O.; Lee, J. H.; Tuller, H. L.; Kim, I. D. Thin-Wall Assembled SnO2Fibers Functionalized by Catalytic Pt Nanoparticles and their Superior Exhaled-Breath-Sensing Properties for the Diagnosis of Diabetes. *Adv. Funct. Mater.* **2013**, *23*, 2357−2367.

(13) Bai, J.; Zhou, B. Titanium dioxide nanomaterials for sensor applications. *Chem. Rev.* **2014**, *114*, 10131−10176.

(14) Irimpan, L.; Deepthy, A.; Krishnan, B.; Kukreja, L.; Nampoori, V.; Radhakrishnan, P. Effect of self assembly on the nonlinear optical characteristics of ZnO thin films. *Opt. Commun.* **2008**, *281*, 2938−2943.

(15) Kundu, S.; Nithiyanantham, U. DNA-mediated fast synthesis of shape-selective ZnO nanostructures and their potential applications in catalysis and dye-sensitized solar cells. *Ind. Eng. Chem. Res.* **2014**, *53*, 13667−13679.

(16) Zheng, J.; Jiang, Z.-Y.; Kuang, Q.; Xie, Z.-X.; Huang, R.-B.; Zheng, L.-S. Shape-controlled fabrication of porous ZnO architectures

and their photocatalytic properties. *J. Solid State Chem.* **2009**, *182*, 115−121.
(17) Öztürk, S.; Kılınç, N.; Öztürk, Z. Z. Fabrication of ZnO nanorods for NO_2 sensor applications: effect of dimensions and electrode position. *J. Alloys Compd.* **2013**, *581*, 196−201.
(18) Lupan, O.; Ursaki, V.; Chai, G.; Chow, L.; Emelchenko, G. A.; Tiginyanu, I.; Gruzintsev, A. N.; Redkin, A. Selective hydrogen gas nanosensor using individual ZnO nanowire with fast response at room temperature. *Sens. Actuators, B* **2010**, *144*, 56−66.
(19) Nimbalkar, A. R.; Patil, M. G. Synthesis of ZnO thin film by sol-gel spin coating technique for H 2 S gas sensing application. *Physica B* **2017**, *527*, 7−15.
(20) Tench, A.; Lawson, T. Oxygen species adsorbed on zinc oxide. *Chem. Phys. Lett.* **1971**, *8*, 177−178.
(21) Katoch, A.; Kim, J.-H.; Kwon, Y. J.; Kim, H. W.; Kim, S. S. Bifunctional Sensing Mechanism of SnO2-ZnO Composite Nanofibers for Drastically Enhancing the Sensing Behavior in H2 Gas. *ACS Appl. Mater. Interfaces* **2015**, *7*, 11351−11358.
(22) Bhati, V. S.; Ranwa, S.; Rajamani, S.; Kumari, K.; Raliya, R.; Biswas, P.; Kumar, M. Improved sensitivity with low limit of detection of a hydrogen gas sensor based on rGO-loaded Ni-doped ZnO nanostructures. *ACS Appl. Mater. Interfaces* **2018**, *10*, 11116−11124.
(23) Kim, J.-H.; Mirzaei, A.; Kim, H. W.; Kim, S. S. Pd functionalization on ZnO nanowires for enhanced sensitivity and selectivity to hydrogen gas. *Sens. Actuators, B* **2019**, *297*, 126693.
(24) Lim, S. K.; Hong, S. H.; Hwang, S.-H.; Choi, W. M.; Kim, S.; Park, H.; Jeong, M. G. Synthesis of Al-doped ZnO nanorods via microemulsion method and their application as a CO gas sensor. *J. Mater. Sci. Technol.* **2015**, *31*, 639−644.
(25) Drønen, K.; Roalkvam, I.; Beeder, J.; Torsvik, T.; Steen, I. H.; Skauge, A.; Liengen, T. Modeling of heavy nitrate corrosion in anaerobe aquifer injection water biofilm: a case study in a flow rig. *Environ. Sci. Technol.* **2014**, *48*, 8627−8635.
(26) Natter, M.; Keevan, J.; Wang, Y.; Keimowitz, A. R.; Okeke, B. C.; Son, A.; Lee, M.-K. Level and degradation of Deepwater Horizon spilled oil in coastal marsh sediments and pore-water. *Environ. Sci. Technol.* **2012**, *46*, 5744−5755.
(27) Liao, L.; Lu, H.; Li, J.; He, H.; Wang, D.; Fu, D.; Liu, C.; Zhang, W. Size dependence of gas sensitivity of ZnO nanorods. *J. Phys. Chem. C* **2007**, *111*, 1900−1903.
(28) Shirage, P. M.; Rana, A. K.; Kumar, Y.; Sen, S.; Leonardi, S.; Neri, G. Sr- and Ni-doping in ZnO nanorods synthesized by a simple wet chemical method as excellent materials for CO and CO2 gas sensing. *RSC Adv.* **2016**, *6*, 82733−82742.
(29) Xuan, J.-Y.; Zhao, G.-D.; Shi, X.-B.; Geng, W.; Li, H.-Z.; Sun, M.-L.; Jia, F.-C.; Tan, S.-G.; Yin, G.-C.; Liu, B. In-situ fabrication of ZnO nanoparticles sensors based on gas-sensing electrode for ppb-level H2S detection at room temperature*. *Chin. Phys. B* **2021**, *30*, 020701.
(30) Liu, L.; Yang, W.; Zhang, H.; Yan, X.; Liu, Y. Ultra-High Response Detection of Alcohols Based on CdS/MoS2 Composite. *Nanoscale Res. Lett.* **2022**, *17*, 7.
(31) Singh, B.; Kaushal, A.; Bdikin, I.; Venkata Saravanan, K. V.; Ferreira, J. Effect of Ni doping on structural and optical properties of Zn1−Ni O nanopowder synthesized via low cost sono-chemical method. *Mater. Res. Bull.* **2015**, *70*, 430−435.
(32) Pal, B.; Sarkar, D.; Giri, P. Structural, optical, and magnetic properties of Ni doped ZnO nanoparticles: correlation of magnetic moment with defect density. *Appl. Surf. Sci.* **2015**, *356*, 804−811.
(33) Bai, S.; Hu, J.; Li, D.; Luo, R.; Chen, A.; Liu, C. C. Quantum-sized ZnO nanoparticles: Synthesis, characterization and sensing properties for NO2. *J. Mater. Chem.* **2011**, *21*, 12288−12294.
(34) Al-Hardan, N.; Abdullah, M.; Aziz, A. A. Performance of Cr-doped ZnO for acetone sensing. *Appl. Surf. Sci.* **2013**, *270*, 480−485.
(35) Li, Z.; Huang, Y.; Zhang, S.; Chen, W.; Kuang, Z.; Ao, D.; Liu, W.; Fu, Y. A fast response & recovery H2S gas sensor based on α-Fe2O3 nanoparticles with ppb level detection limit. *J. Hazard. Mater.* **2015**, *300*, 167−174.
(36) Yang, W.; Tang, J.; Ou, Q.; Yan, X.; Liu, L.; Liu, Y. Recyclable Ag-Deposited TiO2 SERS Substrate for Ultrasensitive Malachite Green Detection. *ACS Omega* **2021**, *6*, 27271−27278.
(37) Kim, J.; Yong, K. Mechanism Study of ZnO Nanorod-Bundle Sensors for H2S Gas Sensing. *J. Phys. Chem. C* **2011**, *115*, 7218−7224.
(38) Modaberi, M. R.; Rooydell, R.; Brahma, S.; Akande, A. A.; Mwakikunga, B. W.; Liu, C.-P. Enhanced response and selectivity of H2S sensing through controlled Ni doping into ZnO nanorods by using single metal organic precursors. *Sens. Actuators, B* **2018**, *273*, 1278−1290.
(39) Ugale, A. D.; Umarji, G. G.; Jung, S. H.; Deshpande, N. G.; Lee, W.; Cho, H. K.; Yoo, J. B. ZnO decorated flexible and strong graphene fibers for sensing NO2 and H2S at room temperature. *Sens. Actuators, B* **2020**, *308*, 127690.
(40) Na, H.-B.; Zhang, X.-F.; Zhang, M.; Deng, Z.-P.; Cheng, X.-L.; Huo, L.-H.; Gao, S. A fast response/recovery ppb-level H2S gas sensor based on porous CuO/ZnO heterostructural tubule via confined effect of absorbent cotton. *Sens. Actuators, B* **2019**, *297*, 126816.
(41) Fan, K.; Guo, J.; Cha, L.; Chen, Q.; Ma, J. Atomic layer deposition of ZnO onto Fe 2 O 3 nanoplates for enhanced H 2 S sensing. *J. Alloys Compd.* **2017**, *698*, 336−340.
(42) Wang, L.; Kang, Y.; Wang, Y.; Zhu, B.; Zhang, S.; Huang, W.; Wang, S. CuO nanoparticle decorated ZnO nanorod sensor for low-temperature H2S detection. *Mater. Sci. Eng., C* **2012**, *32*, 2079−2085.
(43) Gao, Y.; Kong, D.; Han, J.; Zhou, W.; Gao, Y.; Wang, T.; Lu, G. Cadmium sulfide in-situ derived heterostructure hybrids with tunable component ratio for highly sensitive and selective detection of ppb-level H2S. *J. Colloid Interface Sci.* **2022**, *627*, 332−342.
(44) Hu, Q.; Zhang, W.; Wang, X.; Wang, Q.; Huang, B.; Li, Y.; Hua, X.; Liu, G.; Li, B.; Zhou, J.; Xie, E.; Zhang, Z. Binder-free CuO nanoneedle arrays based tube-type sensor for H2S gas sensing. *Sens. Actuators, B* **2021**, *326*, 128993.
(45) Park, K.-R.; Kim, R. N.; Song, Y.; Kwon, J.; Choi, H. Facile Fabrication of ZnO-ZnFe2O4 Hollow Nanostructure by a One-Needle Syringe Electrospinning Method for a High-Selective H2S Gas Sensor. *Materials* **2022**, *15*, 399.
(46) Song, B.-Y.; Zhang, X.-F.; Huang, J.; Cheng, X.-L.; Deng, Z.-P.; Xu, Y.-M.; Huo, L.-H.; Gao, S. Porous Cr_2O_3 Architecture Assembled by Nano-Sized Cylinders/Ellipsoids for Enhanced Sensing to Trace H_2S Gas. *ACS Appl. Mater. Interfaces* **2022**, *14*, 22302.

https://doi.org/10.1021/acsomega.2c07092
ACS Omega 2023, 8, 7595−7601